13th International Workshop on Innovative Simulation for Healthcare, 007
21st International Multidisciplinary Modeling & Simulation Multiconference

2724-0371 © 2024 The Authors.
doi: 10.46354/i3m.2024.iwish.007

Simulating Brain Gradient-Echo Magnetic Resonance Images through Microstructural Modeling

Mert Şişman[1,2], Alexandra Roberts[1,2], Hangwei Zhuang[2,3], Renjiu Hu[2,4], Junghun Cho[5], Shun Zhang[6], Pascal Spincemaille[2], Thanh Nguyen[2] and Yi Wang[2,3,*]

[1]Department of Electrical and Computer Engineering, Cornell University, Ithaca, NY 14850, USA
[2]Department of Radiology, Weill Cornell Medicine, New York, NY 10021, USA
[3]Meinig School of Biomedical Engineering, Cornell University, Ithaca, NY 14850, USA
[4]Sibley School of Mechanical and Aerospace Engineering, Cornell University, Ithaca, NY 14850, USA
[5]Department of Biomedical Engineering, State University of New York at Buffalo, Buffalo, NY 14228, USA
[6]Tongji Hospital, Tongji Medical College, Huazhong University of Science and Technology Wuhan, China

*Corresponding author. Email address: yiwang@med.cornell.edu

Abstract

Quantitative magnetic resonance imaging (qMRI) methods usually suffer from the lack of appropriate or easy-to-implement methods of validation. Here, we developed a detailed framework to synthetically generate realistic brain multi gradient-echo (mGRE) data incorporating biophysical modeling of the MRI signals and microstructure brain tissues. In addition to validation, simulated data can also be utilized for the supervised training of deep learning models for the inverse mapping of the microstructural and physiological distributions. The feasibility of one such parameter that is extremely valuable if can be measured noninvasively, oxygen extraction fraction (OEF), is shown. The simulated and *in vivo* tests demonstrated high accuracy in the mapping. The developed method and the results reflect the significance of simulation-based computational approaches for answering the clinical needs.

Keywords: quantitative MRI (qMRI); quantitative susceptibility mapping (QSM); gradient-echo (GRE); oxygen extraction fraction (OEF)

1. Introduction

Magnetic Resonance Imaging (MRI) is an extremely powerful tool for clinical diagnostics. Although it is one of the most employed discriminators for malignant diseases, most of its effectiveness was limited to qualitative imaging. Recently, quantitative MRI (qMRI) emerged as a strong candidate for the detection and monitoring of tissue changes (Keenan et al., 2019).

qMRI encapsulates a large collection of MRI methodologies including but not limited to diffusion-weighted imaging (Jones & Leemans, 2011; Le Bihan et al., 1992), T1/T2 mapping either using special pulse sequences (Ben-Eliezer et al., 2015; Stikov et al., 2015) or MRI fingerprinting (Ma et al., 2013), quantitative susceptibility mapping (QSM) (Wang & Liu, 2015), and myelin water fraction (MWF) imaging (MacKay et al., 1994). Although these qMRI tools carry significant potential, their success is limited by feasibility, repeatability, and most importantly accuracy. Therefore, there is a need for validation of the

developed methods. For instance, some studies utilize histology for the validation of QSM (Gillen et al., 2018) and MWF imaging (Laule et al., 2008). However, it is not possible to apply histological validation for certain MRI measurements such as T1/T2 mapping. Therefore, a validation tool that is comprehensive to all MRI measurements in addition to being compatible with the biophysical mechanisms governing the MRI signal generation can be extremely beneficial. With the development of highly efficient and strong computational tools, *in silico* validation becomes a strong candidate.

However, simulation MRI data carries a high potential with the increased knowledge of the tissue microstructure and publicly available datasets. It is possible to generate realistic MRI datasets mimicking the physical signal generation processes with known signal source distributions. Furthermore, simulated MRI data is not only beneficial for validation purposes but it also brings up the possibility of utilizing supervised deep learning methods since the labeled data can be automatically generated.

In this study, we developed a framework for the simulation of multi gradient-echo (mGRE) MRI images based on detailed biophysical modeling. Microstructural information such as blood oxygenation-related signal decay and fiber orientation dependent signal variations were included in the model for realistic data generation. In addition, non-idealities such as off-resonance effects present in the real MRI measurements were also incorporated into the simulation. Additionally, the feasibility of training a neural network using the generated data for inverse mapping of oxygen extraction fraction (OEF) was examined.

The remaining sections are organized as following: State-of-the-art section summarizes the previous methods utilized for realistic MRI data generation and OEF estimation from MRI data. Material and Methods section describes the details of the mGRE magnitude and phase simulation, and OEF estimation through supervised training. Results and Discussion section presents the example simulation data, comparison to real MRI data, and the accuracy of the estimated OEF maps. Finally, conclusion section provides the concluding remarks.

2. State-of-the-art

Physics based simulation of realistic MRI data has been employed previously for example for the evaluation of the image processing algorithms (Kwan et al., 1999). Moreover, the SIMRI was designed as an interactive tool for the synthesis of simulated MRI data based on Bloch equations (Benoit-Cattin et al., 2005). Similar to our approach, supervised training

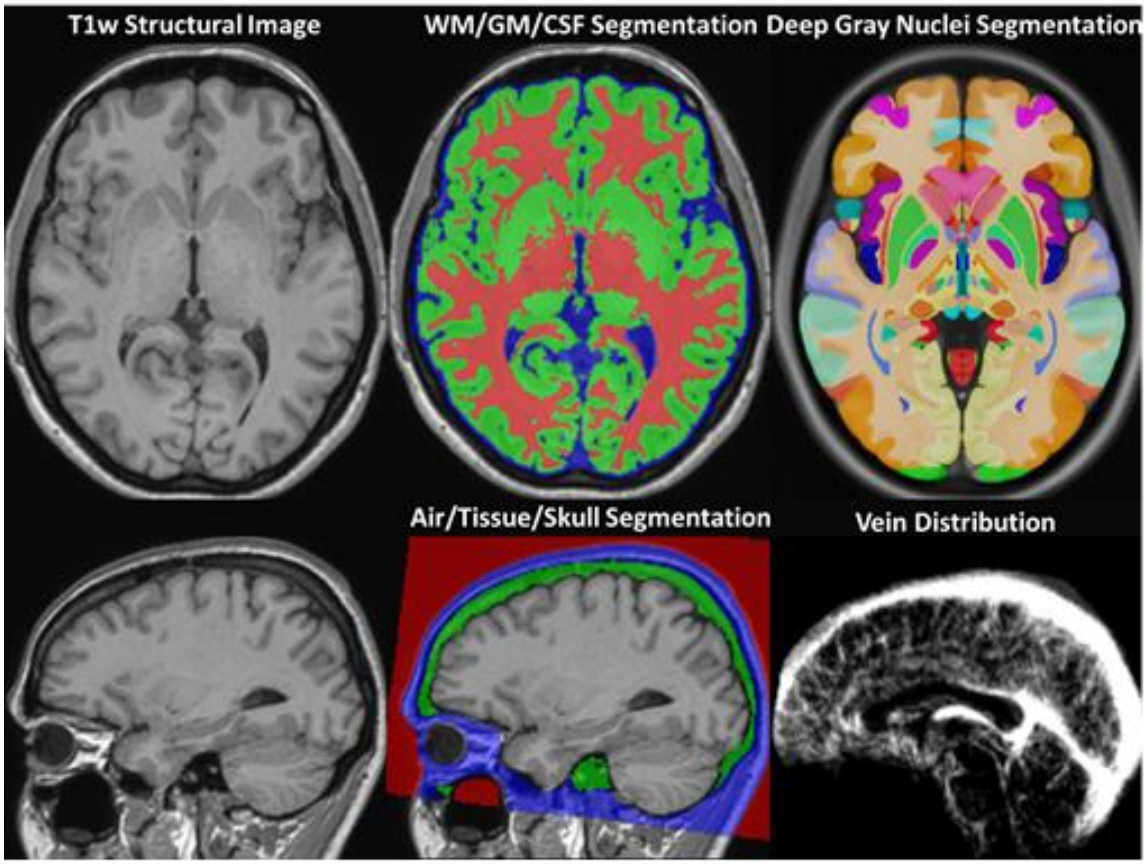

Figure 1. An example of the brain segmentation steps. T1-weighted (T1w) anatomy-defining image and WM/GM/CSF, deep gray nuclei, air/tissue/skull segmentations and the vein partial volume map in the same space obtained through explained steps.

with synthetic MRI data was proposed for image segmentation (Xanthis et al., 2021) and registration tasks (Hoffmann et al., 2022). The accuracy of the deep learning based segmentation methods was previously evaluated (Jany & G.A., 2021).

For MRI based OEF estimation several methods were proposed such as quantitative blood oxygenation-dependent (qBOLD)-OEF (He & Yablonskiy, 2007) and phase-based techniques such as QSM-OEF (Zhang et al., 2017), and combined estimation method called qBOLD-QSM (QQ)-OEF (Cho et al., 2018).

3. Materials and Methods

mGRE data can be considered one of the simplest MRI acquisition schemes, yet it includes the effects of a vast group of signal sources. Fundamentally, mGRE can be described as a signal distribution generated by water protons and modified by various susceptibility sources. Susceptibility effects have long been considered as an artifact source that needs to be corrected for or avoided until qualitative susceptibility-weighted imaging (SWI) (Haacke et al., 2004) and QSM have been shown to provide crucial clinical information.

To simulate mGRE data, magnitude, and phase need to be modeled separately as they present correlated but distinct effects. T1/T2/PD - weighted images from the IXI dataset (http://brain-development.org/ixi-dataset/) were utilized as the baseline for the brain anatomy and tissue segmentations required for the following steps.

3.1. Modeling Phase Signal

The phase of mGRE data mainly reflects the distribution of the susceptibility sources. Therefore, a realistic QSM map for each simulated brain is generated following the described steps in the QSM reconstruction challenge 2.0 (Marques et al., 2021). Certain modifications were adapted due to the anatomical images available in the IXI dataset differing from what was utilized in the challenge data. The segmentation of different tissues and structures was realized as follows:

- White matter (WM), gray matter (GM), and cerebrospinal fluid (CSF) segmentations are obtained using the FSL FAST algorithm (Zhang et al., 2001) and T1/T2/PD - weighted images.
- Deep gray nuclei structures are automatically segmented by non-rigid registration of the Allen brain atlas (Ding et al., 2016) via ANTs *SyN* algorithm (Avants et al., 2009) to the anatomical images.
- Air/tissue/skull regions are automatically segmented by non-rigid registration of tissue probability maps of the Statistical Parametric Mapping (SPM) toolbox (Ashburner, 2009) to the anatomical images.
- The vein partial volume map is obtained through non-rigid registration of the vein atlas provided in (Ward et al., 2018).

An example of the T1-weighted (T1w) structural image and corresponding segmentation maps and vein partial volume distribution is shown in Figure 1. Once the segmentation maps are available, a QSM distribution can be created by assigning distinct susceptibility values to each tissue type. The partial volume between different tissues and intra-tissue modulations were also incorporated following (Marques et al., 2021). For intra-tissue modulations, R1 and R2 maps are simulated by scaling the ratios of T1/PD – weighted and T2/PD – weighted images, respectively. The modulation factors were recalibrated as the original values were provided for R1 and $R2^*$ maps.

An important detail is that the susceptibility of venous blood depends on the oxygen saturation and volume of the venous blood present in each voxel. Venous blood saturation rate can be estimated from an available OEF map and cerebral blood volume (CBV) can be derived from a cerebral blood flow (CBF) map (Zhang et al., 2017). Two in-house datasets were created to randomly generate realistic brain OEF and CBV distributions. For OEF, 15 OEF maps estimated from 15O - Positron Emission Tomography and published in (Cho, Lee, et al., 2021), were non-rigidly registered to Montreal Neurological Institute (MNI)

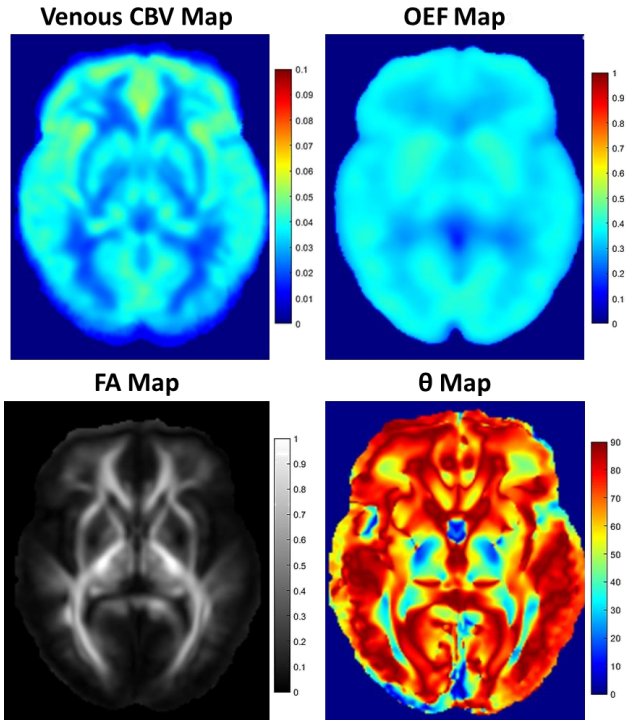

Figure 2. Example CBV, OEF, FA and θ maps in the same space with the images presented in Figure 1.

space. A similar operation was applied to 8 CBV maps derived from the arterial spin labeling (ASL) based CBF maps acquired locally (Buxton, 2005). We utilized a pseudo-continuous arterial spin labeling (PCASL) 3D fast spin echo (FSE) sequence to capture brain data from healthy volunteers (N = 8; four males and four females) using a GE MR750 3T scanner (GE, Milwaukee, WI) equipped with a 32-channel head coil. The imaging parameters were as follows: image voxel dimensions of 128x128x36, image volume size of 1.875x1.875x4 mm^3, echo time of 10.5 ms, single signal average (NEX=1), and a labeling duration of 1450 ms. A post-labeling delay (PLD = 1525 ms) was employed to generate CBF maps. For each simulated brain, these maps were linearly mixed with randomly chosen coefficients and warped into the same space where the previously created tissue maps reside to generate randomized distributions. Once OEF and CBV maps were available in the simulation space, venous susceptibilities were estimated following the equations in (Cho, Spincemaille, et al., 2021).

The field perturbation distribution due to all the simulated susceptibility effects was obtained through discretized dipole convolution (Kee et al., 2017). The final important inclusion in the phase modeling of the mGRE data is the addition of fiber orientation-dependent local field perturbations that do not follow the dipole convolution (Wharton & Bowtell, 2015). The fractional anisotropy (FA) and fiber orientation (θ) maps were estimated from the International Consortium of Brain Mapping (ICBM) DTI-81 normative atlas (Mori et al., 2008) warped into the simulation space. Example CBV, OEF, FA, and θ maps are presented in Figure 2.

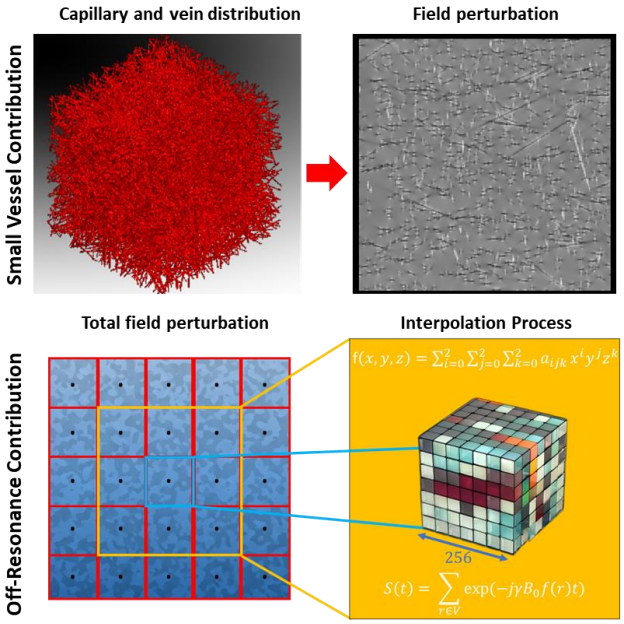

Figure 3. Example simulated volume distribution of small veins inside a voxel with corresponding field perturbation for a given blood oxygenation level (top row). The process to estimate magnitude decay from the intravoxel dephasing. For each voxel, 27 coefficients (a_{ijk}) for a quadratic fit to the local field is estimated from the 3^3 and these coefficients utilized to interpolate the field inside the voxel into 256^3 grid (bottom row). The magnitude signal decay for each voxel is estimated using the complex summation using the superposed field f(r) created by both capillaries and off-resonance. γ is the gyromagnetic ratio of Hydrogen proton, B_0 is the static magnetic field strength of the MR scanner, and t is the independent variable for time.

3.2. Modeling Magnitude Signal

Compared to the phase, magnitude is more sensitive to the local field variations and the dephasing of proton spins should be carefully modeled to accurately reflect magnitude signal decay characteristics. Four main mechanisms that affect mGRE magnitude signal decay are modeled:

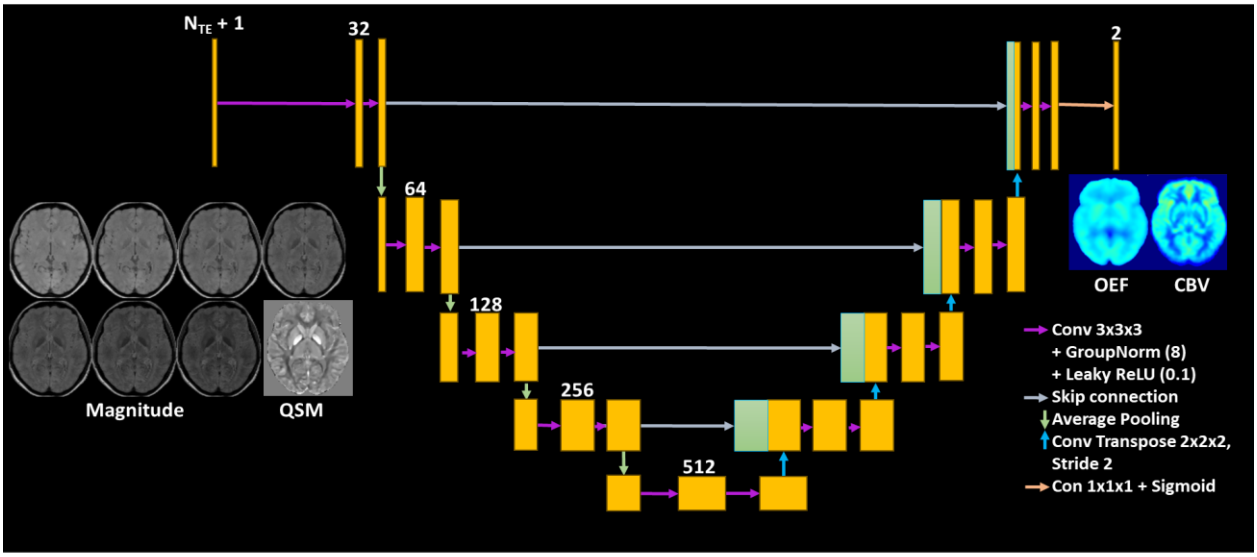

Figure 4. U-net architecture utilized for OEF and CBV estimations.

- Exponential decay with rate $R2^*$ which is the sum of R2 which reflects the dephasing of spin magnetizations due to nanoscopic random motion of water protons and R2′ which accounts for the microscopic dephasing due to susceptibility effects. R2′ is estimated from the simulated QSM map using the relation $R2' = D \times |QSM|$ where D = 137 Hz/ppm (Shin et al., 2021).
- Fiber orientation-dependent signal decay due to the field perturbation created by the myelin sheaths. A myelin volume fraction (MVF) map is created by scaling T1/T2 – weighted images as it is shown that this ratio correlates with myelin content in the brain (Nakamura et al., 2017). Magnitude signal change is simulated following equations derived in (Wharton & Bowtell, 2013).
- Dephasing effects due to the field generated by deoxygenated blood inside the capillaries and small veins. It is simulated numerically by creating a volume composed of randomly oriented and located cylinders whose susceptibility depends on the blood oxygenation level. For different oxygenation levels and cylinder volume fractions, the field perturbations were computed using dipole convolution, and the magnitude decay was estimated by summing the complex MRI signal on a 256^3 grid. Computed curves were stored in a dictionary with the corresponding labels (OEF and CBV) for fast computation afterward. An example volume and the corresponding field distribution are demonstrated in Figure 3 (top row).
- Off-resonance effects due to the non-uniform field distribution within the voxel. The field distribution inside a voxel is not constant which creates intravoxel dephasing. Especially when the field variation is very strong, this effect manifests itself as very strong signal decay. Numerically, this effect can be simulated by computing the field distribution at a much finer grid and then summing the complex signal to emulate MRI signal generation. However, the time and memory complexity increase exponentially. Therefore, here we employed a local quadratic interpolation strategy to artificially zoom in to the finer grid (256^3) from the 3^3 neighborhoods of each voxel. Finally, the estimated field is utilized to compute the magnitude signal decay. This process is visualized in Figure 3 (bottom row).

Further acceleration (for the last 2 steps) to the above process is achieved by creating a dataset (N=30K) of pre-computed voxel signals given OEF, CBV, background susceptibility (defined by QSM map), and 3^3 neighborhood field values. A multi-layer perceptron (MLP) is trained with the pre-computed dataset for the fast estimation of complex mGRE signals. To guarantee the smoothness of the output, both the phase and the natural logarithm of the magnitude were forced to be 3^{rd} order polynomials by simply estimating the polynomial coefficients by the network. The MLP had 5 layers with ReLU activation function and (30,64,64,64,6) neurons in each layer. The final layer outputs the polynomial coefficients excluding constant value (assuming unit magnitude and zero phase at t=0). It is trained for 1e6 epochs using mean-square error (MSE) loss and 75% training and 25% validation split with learning rate 1e-5.

3.3. Inverse Mapping of OEF Using Simulated Data

As discussed before, the generated data can be utilized for the supervised training of a neural network for the inverse mapping of signal source distributions such as OEF and CBV. Following the QSM + quantitative blood oxygenation level-dependent signal modeling of mGRE data (Cho, Spincemaille, et al., 2021), a 3D U-net (Ronneberger et al., 2015) was trained. The magnitude of mGRE data and the reconstructed QSM map were utilized as input maps concatenated in the channel dimension, and OEF and CBV maps were estimated in the output layer. The QSM map is reconstructed using the maximum spherical mean value filtering (mSMV) algorithm (Roberts et al., 2024) to get the whole-brain QSM and mimic the in vivo data processing. The employed U-net architecture is demonstrated in Figure 4. The training and validation data consisted of 40 and 10 simulated mGRE data and corresponding OEF and CBV maps, respectively. It is trained for 1000 epochs with MSE loss and 1e-4 learning rate. The network weights with the smallest validation loss were saved and used for further analysis. Complex Gaussian noise is added to the simulated mGRE data before training.

Simulated mGRE data were compared with real MRI data. The OEF estimation results were evaluated using an additional simulated test case, a healthy dataset from a healthy subject with both mGRE and 150-PET OEF, and a stroke patient mGRE scan. The acquisition details for the healthy subject and stroke patient can be found in (Wu et al., 2021) and (Cho, Spincemaille, et al., 2021), respectively.

4. Results and Discussion

The simulated field maps through the QSM simulation and dipole convolution process are shown in Figure 5. The tissue field reflects the magnetic field perturbation due to the susceptibility sources inside the brain tissue. The microstructural field demonstrates the field perturbation in the white matter that cannot be simply explained by the local sources. Background field which is in general an order of magnitude larger than the tissue field is generated by the susceptibility sources outside of the brain.

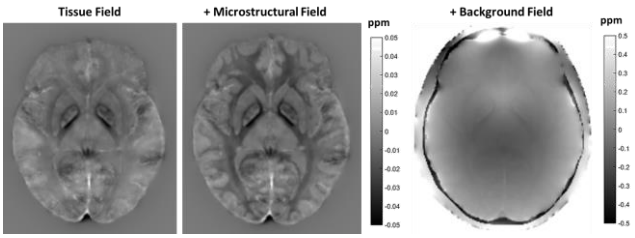

Figure 5. The simulated field from brain tissue components only (tissue field), including microstructural field, and including the background field (field caused by air tissue interfaces).

Three examples of complex mGRE signals estimated via the MLP are given in Figure 6. As can be seen, the predictions do not match with the truths perfectly, even though the smoothness of the data is preserved. When the signal magnitude decays to the signal floor, the truth signal presents a random pattern, the network predictions, on the other hand, preserve a well-behaved pattern in both magnitude and phase. The accuracy needs to be improved by further training with more data.

Figure 7 depicts an example of the simulated mGRE data. Magnitude data presents T1 weighting in the first echo and with increasing echo times, $R2^*$ decay dominates. Microstructural and off-resonance effects manifest with later echoes as well. Phase on the other hand carries mainly the information coming from the simulated QSM and field maps.

In Figure 8, example slices from a reconstructed QSM map from the simulated mGRE data in Figure 7 are shown. There are three benefits of reconstructing QSM back from the final simulated data rather than direct usage of the initial simulated QSM. First, the microstructural field can be included in the data after dipole convolution. Secondly, the reconstructed map shares the same image quality as the QSM map obtained through the same reconstruction from *in vivo* data. Finally, the added complex Gaussian noise aligns with the real measurements better than any noise added to QSM directly.

To evaluate the effectiveness of the proposed mGRE simulation method, real mGRE data from 5 healthy subjects were acquired. Acquired results as well as 5 simulation examples were registered to the MNI standard space in which pairwise structural similarity index measures (SSIM) were calculated both for the combined magnitude and QSM images using only the brain regions (excluding skull and skin). Figure 9 shows example images from both real and simulated data and the heatmap for pairwise comparisons of the all data. Upper half of the heatmap is used for the magnitude comparisons whereas the bottom half presents the QSM comparisons. Visually both magnitude and QSM images seem to show high correlation except for some minor differences such as on the skin. This difference is majorly coming from the unmodeled MRI properties that can be addressed in the future. Quantitatively, QSM maps have comparable SSIM scores between real and simulated

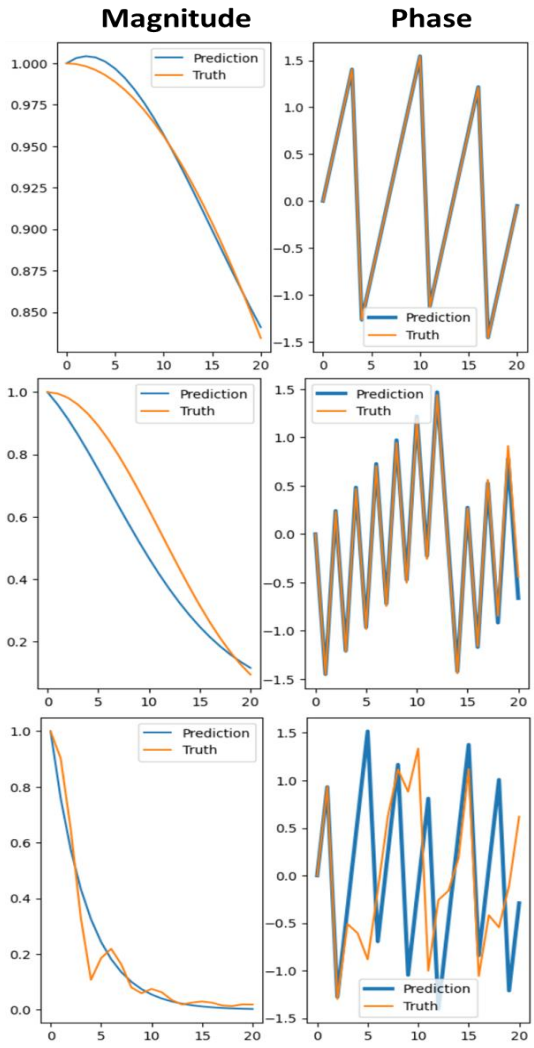

Figure 6. Examples from mGRE signal generation from the trained MLP. Each row represents the magnitude and phase of the mGRE signal corresponding to a single voxel of the simulated data.

data with the SSIM scores real data have with each other. Magnitude on the other hand has relatively low

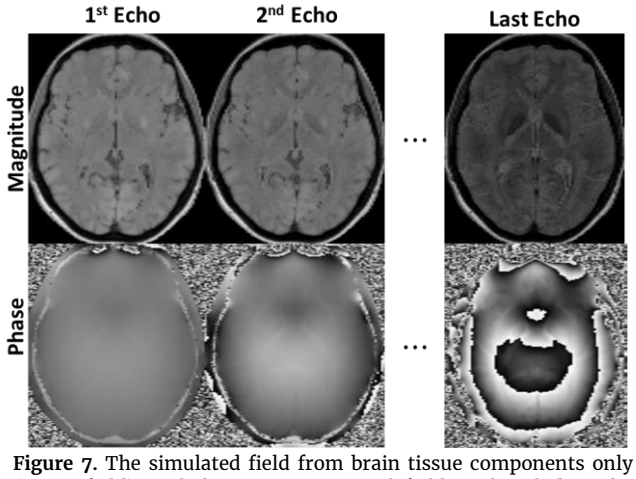

Figure 7. The simulated field from brain tissue components only (tissue field), including microstructural field, and including the background field (field caused by air tissue interfaces).

scores compared to the real QSM data have with each other. However, for magnitude data, simulation and real data similarity is relatively lower (upper right quadrant). Even though the difference is not extremely high (0.72 vs 0.85), this result shows that more improvements in the magnitude is necessary.

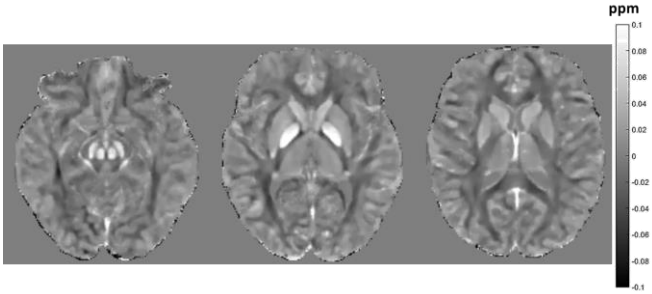

Figure 8. The reconstructed QSM map from the simulated mGRE data using mSMV.

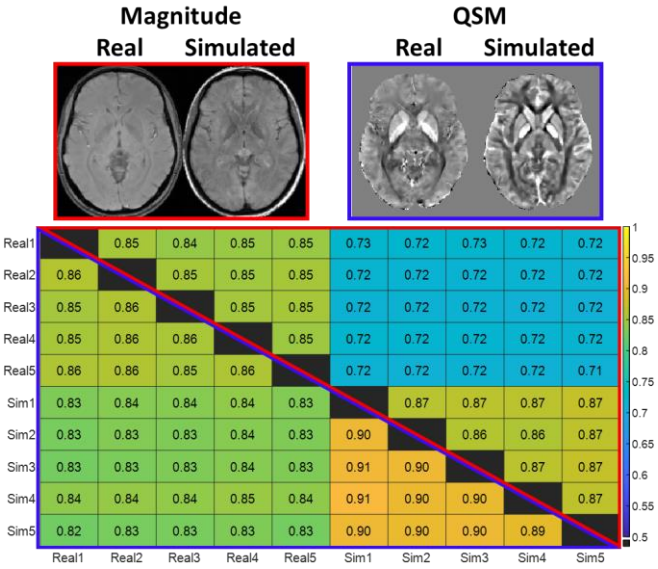

Figure 9. Comparison of real and simulated mGRE data. 5 real cases are acquired from different subjects and compared with 5 simulated brains. Each box shows the SSIM between the two magnitude (upper half) or two QSM (bottom half) images only in the brain regions.

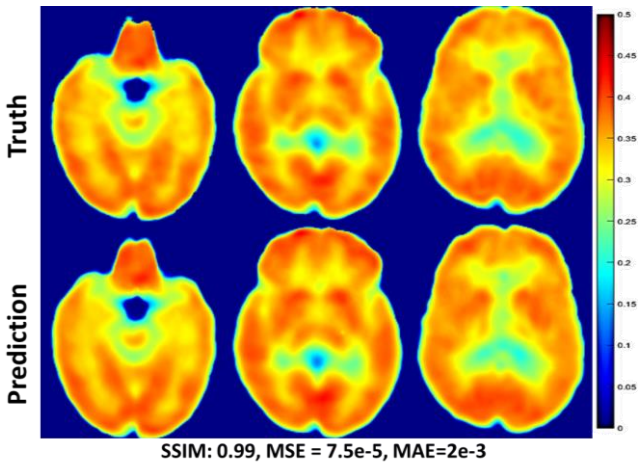

Figure 10. The true and predicted OEF distributions of the simulated test case. SSIM: Structural similarity, MSE: Mean squared error, MAE: Mean absolute error.

The estimated OEF map from the simulated test case is demonstrated in Figure 10 as well as the true distribution. As quantitative metrics, SSIM, mean squared error (MSE) and mean absolute error (MAE) are also given. The maps visually show perfect consistency while quantitative metrics support it. This example suggests that the network is capable of estimating the OEF map accurately for the simulated data.

Figure 11 presents the performance of the trained network on *in vivo* data. Similar to the simulated test case, the network performs very well with the *in vivo* data as well. The 15O-PET based and the network-predicted OEF maps show similar distributions except for a certain level of underestimation in the occipital lobe in the predicted map. The quantitative metrics again show a high level of consistency between the two maps.

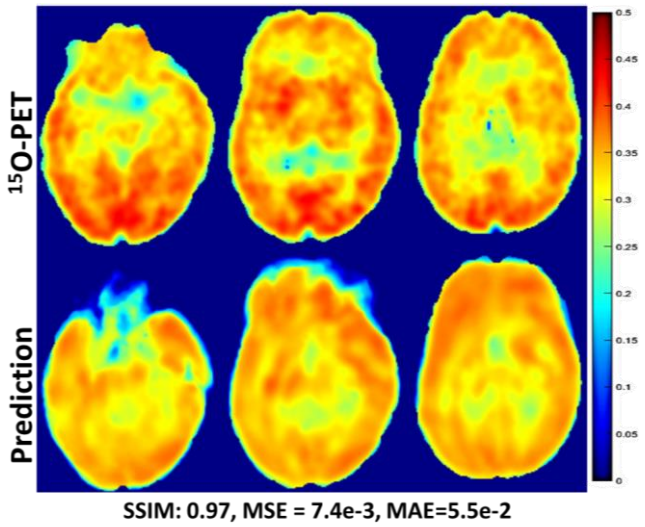

Figure 11. The 15O-PET based and the predicted OEF distributions of the *in vivo* test case. Prediction map is estimated purely from measured mGRE data. SSIM: Structural similarity, MSE: Mean squared error, MAE: Mean absolute error.

Finally, the estimated OEF maps from the mGRE data collected from a stroke patient 58 hours, and 9 days after stroke onset are shown in Figure 12 in addition to the diffusion-weighted images (DWI) and T2-FLAIR. DWI and T2FLAIR show the stroke lesion clearly at the early time point and the corresponding OEF map also presents the decreased OEF in the lesion. In the second time point, the patient shows significant recovery and the OEF map supports it.

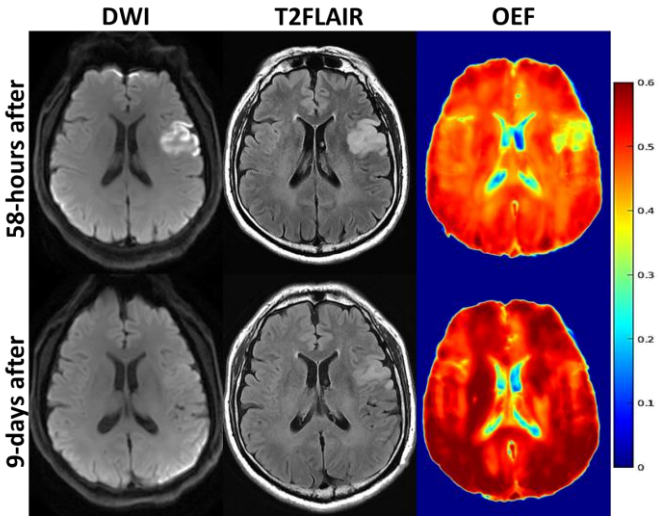

Figure 12. The DWI and T2FLAIR structural images and the estimated OEF maps of a stroke patient 58 hours and 9 days after stroke onset.

5. Conclusions

In this study, we presented a novel way to simulate MRI mGRE data using prior structural information and designed microstructural and physiological distributions. The developed framework can be utilized for *in silico* validation for qMRI acquisition/reconstruction methods as well as supervised training of deep learning models as shown here. The neural network trained to estimate OEF distribution from noninvasive MRI data showed high accuracy in simulation and high consistency with the reference gold-standard ^{15}O-PET based OEF map. Furthermore, it successfully showed the stroke lesion where tissue oxygenation is interrupted. The proposed method can be utilized in the clinical procedures as a noninvasive OEF estimation method. The simulated mGRE data magnitude can potentially be improved to present more similarity with the real MRI data. Future studies will focus on ways to increase the accuracy and efficiency of the developed methods. For instance, physical modeling of blood flow can also be incorporated for increased accuracy of the model such as using computational fluid dynamics (CFD) (Fragomeni, 2023).

Funding

This work was supported in part by research grants from the NIH: R01NS105144, R01NS090464, R01NS095562, S10OD021782, R01HL151686, and National MS Society: RG-1602-07671.

References

Ashburner, J. (2009). Computational anatomy with the SPM software. Magn Reson Imaging, 27(8), 1163-1174.

Avants, B. B., Tustison, N., & Song, G. (2009). Advanced normalization tools (ANTS). Insight j, 2(365), 1-35.

Ben-Eliezer, N., Sodickson, D. K., & Block, K. T. (2015). Rapid and accurate T2 mapping from multi-spin-echo data using Bloch-simulation-based reconstruction. Magn Reson Med, 73(2), 809-817.

Benoit-Cattin, H., Collewet, G., Belaroussi, B., Saint-Jalmes, H., & Odet, C. (2005). The SIMRI project: a versatile and interactive MRI simulator. J Magn Reson, 173(1), 97-115.

Buxton, R. B. (2005). Quantifying CBF with arterial spin labeling. J Magn Reson Imaging, 22(6), 723-726.

Cho, J., Kee, Y., Spincemaille, P., Nguyen, T. D., Zhang, J., Gupta, A.,...Wang, Y. (2018). Cerebral metabolic rate of oxygen (CMRO2) mapping by combining quantitative susceptibility mapping (QSM) and quantitative blood oxygenation level-dependent imaging (qBOLD). Magn Reson Med, 80(4), 1595-1604.

Cho, J., Lee, J., An, H., Goyal, M. S., Su, Y., & Wang, Y. (2021). Cerebral oxygen extraction fraction (OEF): Comparison of challenge-free gradient echo QSM+qBOLD (QQ) with (15)O PET in healthy adults. J Cereb Blood Flow Metab, 41(7), 1658-1668.

Cho, J., Spincemaille, P., Nguyen, T. D., Gupta, A., & Wang, Y. (2021). Temporal clustering, tissue composition, and total variation for mapping oxygen extraction fraction using QSM and quantitative BOLD. Magn Reson Med, 86(5), 2635-2646.

Ding, S. L., Royall, J. J., Sunkin, S. M., Ng, L., Facer, B. A., Lesnar, P.,...Lein, E. S. (2016). Comprehensive cellular-resolution atlas of the adult human brain. J Comp Neurol, 524(16), 3127-3481.

Fragomeni, G. (2023). Newtonian and non-Newtonian blood model, a comparative study on large and small vessels. 20th International Multidisciplinary Modeling & Simulation Multiconference, 12th International Workshop on Innovative Simulation for Healthcare, Athens, Greece.

Gillen, K. M., Mubarak, M., Nguyen, T. D., & Pitt, D. (2018). Significance and In Vivo Detection of Iron-Laden Microglia in White Matter Multiple Sclerosis Lesions. Front Immunol, 9, 255.

Haacke, E. M., Xu, Y., Cheng, Y. C., & Reichenbach, J. R. (2004). Susceptibility weighted imaging (SWI). Magn Reson Med, 52(3), 612-618.

He, X., & Yablonskiy, D. A. (2007). Quantitative BOLD: mapping of human cerebral deoxygenated blood volume and oxygen extraction fraction: default state. Magn Reson Med, 57(1), 115-126.

Hoffmann, M., Billot, B., Greve, D. N., Iglesias, J. E., Fischl, B., & Dalca, A. V. (2022). SynthMorph:

Learning Contrast-Invariant Registration Without Acquired Images. IEEE Trans Med Imaging, 41(3), 543-558.

Jany, J., & G.A., Z. (2021). Practicable Paradigms for Semi-Automated Expert-User Post-Processing of Deep-Learning Segmentations in 3D Radiology. 18th International Multidisciplinary Modeling & Simulation Multiconference, 10th International Workshop on Innovative Simulation for Healthcare, Virtual Event.

Jones, D. K., & Leemans, A. (2011). Diffusion tensor imaging. Methods Mol Biol, 711, 127-144.

Kee, Y., Liu, Z., Zhou, L., Dimov, A., Cho, J., de Rochefort, L.,...Wang, Y. (2017). Quantitative Susceptibility Mapping (QSM) Algorithms: Mathematical Rationale and Computational Implementations. IEEE Trans Biomed Eng, 64(11), 2531-2545.

Keenan, K. E., Biller, J. R., Delfino, J. G., Boss, M. A., Does, M. D., Evelhoch, J. L.,...Sullivan, D. C. (2019). Recommendations towards standards for quantitative MRI (qMRI) and outstanding needs. J Magn Reson Imaging, 49(7), e26-e39.

Kwan, R. K., Evans, A. C., & Pike, G. B. (1999). MRI simulation-based evaluation of image-processing and classification methods. IEEE Trans Med Imaging, 18(11), 1085-1097.

Laule, C., Kozlowski, P., Leung, E., Li, D. K., Mackay, A. L., & Moore, G. R. (2008). Myelin water imaging of multiple sclerosis at 7 T: correlations with histopathology. Neuroimage, 40(4), 1575-1580.

Le Bihan, D., Turner, R., Douek, P., & Patronas, N. (1992). Diffusion MR imaging: clinical applications. AJR Am J Roentgenol, 159(3), 591-599.

Ma, D., Gulani, V., Seiberlich, N., Liu, K., Sunshine, J. L., Duerk, J. L., & Griswold, M. A. (2013). Magnetic resonance fingerprinting. Nature, 495(7440), 187-192.

MacKay, A., Whittall, K., Adler, J., Li, D., Paty, D., & Graeb, D. (1994). In vivo visualization of myelin water in brain by magnetic resonance. Magn Reson Med, 31(6), 673-677.

Marques, J. P., Meineke, J., Milovic, C., Bilgic, B., Chan, K. S., Hedouin, R.,...Schweser, F. (2021). QSM reconstruction challenge 2.0: A realistic in silico head phantom for MRI data simulation and evaluation of susceptibility mapping procedures. Magn Reson Med, 86(1), 526-542.

Mori, S., Oishi, K., Jiang, H., Jiang, L., Li, X., Akhter, K.,...Toga, A. W. (2008). Stereotaxic white matter atlas based on diffusion tensor imaging in an ICBM template. Neuroimage, 40(2), 570-582.

Nakamura, K., Chen, J. T., Ontaneda, D., Fox, R. J., & Trapp, B. D. (2017). T1-/T2-weighted ratio differs in demyelinated cortex in multiple sclerosis. Ann Neurol, 82(4), 635-639.

Ronneberger, O., Fischer, P., & Brox, T. (2015). U-Net: Convolutional Networks for Biomedical Image Segmentation. Medical Image Computing and Computer-Assisted Intervention – MICCAI 2015, Cham.

Shin, H. G., Lee, J., Yun, Y. H., Yoo, S. H., Jang, J., Oh, S. H.,...Choi, H. J. (2021). χ-separation: Magnetic susceptibility source separation toward iron and myelin mapping in the brain. Neuroimage, 240, 118371.

Stikov, N., Boudreau, M., Levesque, I. R., Tardif, C. L., Barral, J. K., & Pike, G. B. (2015). On the accuracy of T1 mapping: searching for common ground. Magn Reson Med, 73(2), 514-522.

Wang, Y., & Liu, T. (2015). Quantitative susceptibility mapping (QSM): decoding MRI data for a tissue magnetic biomarker. Magnetic resonance in medicine, 73(1), 82-101.

Ward, P. G. D., Ferris, N. J., Raniga, P., Dowe, D. L., Ng, A. C. L., Barnes, D. G., & Egan, G. F. (2018). Combining images and anatomical knowledge to improve automated vein segmentation in MRI. Neuroimage, 165, 294-305.

Wharton, S., & Bowtell, R. (2013). Gradient echo based fiber orientation mapping using R2* and frequency difference measurements. Neuroimage, 83, 1011-1023.

Wharton, S., & Bowtell, R. (2015). Effects of white matter microstructure on phase and susceptibility maps. Magn Reson Med, 73(3), 1258-1269.

Wu, D., Zhou, Y., Cho, J., Shen, N., Li, S., Qin, Y.,...Wang, Y. (2021). The Spatiotemporal Evolution of MRI-Derived Oxygen Extraction Fraction and Perfusion in Ischemic Stroke. Front Neurosci, 15, 716031.

Xanthis, C. G., Filos, D., Haris, K., & Aletras, A. H. (2021). Simulator-generated training datasets as an alternative to using patient data for machine learning: An example in myocardial segmentation with MRI. Comput Methods Programs Biomed, 198, 105817.

Zhang, J., Zhou, D., Nguyen, T. D., Spincemaille, P., Gupta, A., & Wang, Y. (2017). Cerebral metabolic rate of oxygen (CMRO2) mapping with hyperventilation challenge using quantitative susceptibility mapping (QSM). Magn Reson Med, 77(5), 1762-1773.

Zhang, Y., Brady, M., & Smith, S. (2001). Segmentation of brain MR images through a hidden Markov random field model and the expectation-maximization algorithm. IEEE Trans Med Imaging, 20(1), 45-57.